

Zhao, J.; Özgen-Xian, I.; Liang, D.; Wang, T.; Hinkelmann, R.

# An improved multislope MUSCL scheme for solving shallow water equations on unstructured grids

Journal article | Accepted manuscript (Postprint)

This version is available at <https://doi.org/10.14279/depositonce-8415>



Zhao, J., Özgen-Xian, I., Liang, D., Wang, T., & Hinkelmann, R. (2019). An improved multislope MUSCL scheme for solving shallow water equations on unstructured grids. *Computers & Mathematics with Applications*, 77(2), 576–596. <https://doi.org/10.1016/j.camwa.2018.09.059>

## Terms of Use

Copyright applies. A non-exclusive, non-transferable and limited right to use is granted. This document is intended solely for personal, non-commercial use.

WISSEN IM ZENTRUM  
UNIVERSITÄTSBIBLIOTHEK

Technische  
Universität  
Berlin

# An improved multislope MUSCL scheme for solving shallow water equations on unstructured grids

Jiaheng Zhao<sup>a</sup>, Ilhan Özgen–Xian<sup>a</sup>, Dongfang Liang<sup>b</sup>, Tian Wang<sup>a,c</sup>,  
Reinhard Hinkelmann<sup>a</sup>

<sup>a</sup>*Chair of Water Resources Management and Modeling of Hydrosystems, Technische Universität Berlin, Germany*

<sup>b</sup>*Department of Engineering, University of Cambridge, Cambridge, UK*

<sup>c</sup>*Institute of Water Resources and Hydro-Electric Engineering, Xi'an University of Technology, Xi'an 710048, China*

---

## Abstract

This paper describes an improved vector manipulation multislope monotone upstream-centred scheme for conservation laws (MUSCL) reconstruction for solving the shallow water equations on unstructured grids. This improved MUSCL reconstruction method includes a bigger stencil for the interpolation and saves time for determining the geometric relations compared to the original vector manipulation method, so it is computationally more efficient and straightforward to implement. Four examples involving an analytical solution, laboratory experiments and field-scale measurements are used to test the performance of the proposed scheme. It has been proven that the proposed scheme can provide comparable accuracy and higher efficiency compared to the original vector manipulation method. With the increasing of the number of cells, the advantage of the proposed scheme becomes more apparent.

*Keywords:* finite volume method, MUSCL scheme, shallow water, total variation diminishing, unstructured grids

---

1 **Highlights**

- 2 1. An improved vector manipulation multislope MUSCL method is pre-  
3 sented on unstructured grids with the aim of better accuracy and higher  
4 efficiency
- 5 2. The improved scheme includes a bigger stencil for the interpolation and  
6 is more straightforward to implement than the original method
- 7 3. The numerical model shows good agreement with measurements as long  
8 as the shallow flow assumptions are satisfied

9 **1. Introduction**

10 Monotone upstream-centred scheme for conservation laws (MUSCL) [1] is  
11 a well-known approach for achieving high-order accuracy by data reconstruc-  
12 tion for solving hyperbolic partial differential equations. In hydrodynamics,  
13 many researchers use the MUSCL scheme to solve the two-dimensional shal-  
14 low water equations (SWEs) due to its monotonicity and high order accuracy  
15 (e.g. [2, 3, 4, 5]). The MUSCL-type schemes are an extension of the original  
16 Godunov scheme [6]. The variable values along the cell edges are extrapolated  
17 from the cell centres, and the reconstructed values are stored at the edges  
18 to calculate the Riemann flux across the edges. In order to avoid spurious  
19 oscillations and produce physically meaningful results, the numerical scheme  
20 should be monotonic. The monotonic numerical scheme can be deduced by  
21 examining the total variation, which is defined as an over time decreasing  
22 summation of the differences between each all adjacent cells.

23 Early TVD schemes were derived on structured grids. Directly applying  
24 them on unstructured grids often leads to poor results, because the structured  
25 grid provides a simple stencil layout for figuring out the upwind and down-  
26 wind neighbors. On unstructured grids, the upwind and downwind neighbors  
27 are often not located along the perpendicular bisector of the edge. This has  
28 to be accounted for in MUSCL reconstructions on unstructured grids.

29 On unstructured grids, TVD MUSCL schemes can be divided into monos-  
30 slope and multislope methods [2]. The monoslope method was initially pre-  
31 sented in [7], which calculates a single slope for the entire cell based on the  
32 three immediate neighbors of the cell [8]. The multislope method calculates  
33 a slope for each edge based on a three-point stencil. Stencils are set up based  
34 on the extrapolation in the upwind direction, and the variable values at the  
35 upwind point can be interpolated [9], [4], or set to the value at the cell centre  
36 that is closest to the perpendicular bisector of the considered edge. These  
37 methods require significant computational effort to determine the upwind  
38 cells and the upwind point in the stencil. A poor choice of the upwind point  
39 introduces significant numerical errors, even leading to the loss of the TVD  
40 property.

41 As discussed in Hou *et al.* [5], the multislope method can provide a more  
42 efficient and straightforward scheme. Although the multislope method may  
43 not provide a piecewise linear slope for the considered cell, the reconstructed  
44 values only determine the fluxes across the edges and thus will not influence  
45 the conservation law. Therefore, the shape of the reconstructed function  
46 inside the cell is not of importance for the FVM [5].

47 The vector based manipulation method is proposed by Buffard and Clain

48 [2], who provide a very straightforward method on complex unstructured  
 49 grids, especially suitable for multi-dimensional schemes. Based on the idea  
 50 of Buffard and Clain [2], Hou *et al.* [5] proposed a new vector based manipu-  
 51 lation multislope method. However, in the authors' previous work [8], it was  
 52 found that their scheme [5] does not include enough downwind information  
 53 for the calculation of the downwind slopes, which may lead to the wrong  
 54 interpolation. In order to overcome this problem, Zhao *et al.* [8] calculates  
 55 the down-slope value in the downwind direction, which increases the robust-  
 56 ness and accuracy. A new multislope MUSCL method is devised in this work  
 57 to improve the accuracy, which includes more stencil points to maintain the  
 58 monotonicity of the scheme in different flow conditions.

59 This study is based on the framework of unstructured Godunov-type cell-  
 60 centered FVM. The new MUSCL scheme is compared with the scheme in [8]  
 61 and analytical analyses.

## 62 2. Governing equations and numerical model

63 The two-dimensional shallow water equations (SWEs) are derived from  
 64 the depth-averaged Navier-Stokes equations. They can be written in the  
 65 conservative vector form as:

$$\frac{\partial \mathbf{q}}{\partial t} + \frac{\partial \mathbf{f}}{\partial x} + \frac{\partial \mathbf{g}}{\partial y} = \mathbf{s} \quad (1)$$

66 with vectors defined as

$$\mathbf{q} = \begin{bmatrix} h \\ q_x \\ q_y \end{bmatrix}, \quad \mathbf{f} = \begin{bmatrix} q_x \\ uq_x + gh^2/2 \\ uq_y \end{bmatrix}, \quad \mathbf{g} = \begin{bmatrix} q_y \\ vq_x \\ vq_y + gh^2/2 \end{bmatrix}, \quad (2)$$

$$\mathbf{s} = \begin{bmatrix} 0 \\ -gh\frac{\partial z}{\partial x} - c_f u \sqrt{u^2 + v^2} \\ -gh\frac{\partial z}{\partial y} - c_f v \sqrt{u^2 + v^2} \end{bmatrix}, \quad (3)$$

68 where  $x$  and  $y$  are the Cartesian coordinates,  $t$  is time,  $\mathbf{q}$  represents the  
 69 unknown variable vector consisting of  $h$ ,  $q_x$  and  $q_y$  denoting the water depth,  
 70 unit-width discharges in  $x$ - and  $y$ - direction, respectively.  $u$ ,  $v$  are defined  
 71 as depth-averaged velocities in  $x$ - and  $y$ -direction, respectively;  $\mathbf{f}$  and  $\mathbf{g}$  are  
 72 the flux vectors in  $x$ - and  $y$ -direction, respectively;  $\mathbf{s}$  is the source term that  
 73 includes bed slope and friction contributions,  $z$  is the bed elevation and  $c_f$   
 74 is the bed roughness coefficient calculated as  $gn^2/h^{1/3}$ ,  $g$  is the gravitational  
 75 acceleration. Viscous and turbulent flux terms are neglected in this equation.

### 76 2.1. Finite volume discretization of SWEs on unstructured grids

77 The shallow water equations(SWEs) in Eq. (1) can be integrated over a  
 78 cell as

$$\int_{\Omega} \frac{\partial \mathbf{q}}{\partial t} d\Omega + \int_{\Omega} \left( \frac{\partial \mathbf{f}}{\partial x} + \frac{\partial \mathbf{g}}{\partial y} \right) d\Omega = \int_{\Omega} \mathbf{s} d\Omega, \quad (4)$$

79 where  $\Omega$  denotes the area of a cell. Applying the divergence theorem and  
 80 replacing the boundary integral with a sum over all edges, Eq. (4) becomes

$$\int_{\Omega} \frac{\partial \mathbf{q}}{\partial t} d\Omega + \sum_{k=1}^m \mathbf{F} \cdot \mathbf{n}_k l_k = \int_{\Omega} \mathbf{s} d\Omega, \quad (5)$$

81 herein  $m$  is the number of edges,  $l$  is the length of the edge, and  $\mathbf{n} = (n_x, n_y)^T$ ,  
 82 is the unit normal vector pointing in the outward normal direction of the  
 83 boundary edge,  $\mathbf{F} \cdot \mathbf{n}$  is the flux vector normal to the boundary and can be

84 written as

$$\mathbf{F} \cdot \mathbf{n} = (\mathbf{f}\mathbf{n}_x + \mathbf{g}\mathbf{n}_y) = \begin{bmatrix} q_x n_x + q_y n_y \\ (u q_x + g h^2 / 2) n_x + v q_y n_y \\ u q_x n_x + (v q_y + g h^2 / 2) n_y \end{bmatrix}. \quad (6)$$

85 The value of  $\mathbf{q}$  in cell  $i$  is updated using the two-stage explicit Runge-  
86 Kutta scheme [10, 11, 12], where the value at the next time level in cell  $i$ ,  
87  $\mathbf{q}_i^{n+1}$ , is updated by

$$\mathbf{q}_i^{n+1} = \frac{1}{2} \{ \mathbf{q}_i^n + \kappa [ \kappa ( \mathbf{q}_i^n ) ] \}, \quad (7)$$

88 with

$$\kappa(\mathbf{q}_i^n) = \mathbf{q}_i^n + \frac{\Delta t}{\Omega} \left[ \int_{\Omega} \mathbf{s} d\Omega - \sum_{k=1}^m \mathbf{F}(\mathbf{q}_i^n)_k \cdot \mathbf{n}_k l_k \right], \quad (8)$$

89 where  $\kappa$  is a function to represent the updating process to a new time level  
90 in the considered cell.  $\Delta t$  is the time step. For this work, the Courant-  
91 Friedrichs-Lewy condition is followed for maintaining the stability,

$$\Delta t = \text{CFL} \min \left( \frac{R_1}{\sqrt{u_1^2 + v_1^2 + \sqrt{gh_1}}}, \dots, \frac{R_n}{\sqrt{u_n^2 + v_n^2 + \sqrt{gh_n}}} \right), \quad (9)$$

92 where  $R_n$  is the minimum distance from the cell center to the edge, CFL is  
93 the Courant-Friedrichs-Lewy number. For explicit time marching algorithms  
94  $\text{CFL} \in (0, 1]$ . In this work,  $\text{CFL} = 0.5$  is adopted.

### 95 **3. Multislope MUSCL reconstruction methods**

96 The original Godunov's theorem used cell-averaged values for calculating  
97 the flux and slope source terms. This is first order accurate. In order to get  
98 higher accuracy, a linear MUSCL reconstruction is usually used to obtain  
99 a second-order accurate scheme. Different ways for calculating slopes lead

100 to different types of MUSCL reconstructions that give different performance  
101 (cf., e.g., [13, 14, 15, 12, 16, 17, 18]). In the multislope method, slopes are  
102 calculated towards each edge individually. As shown in Fig. 1, reconstructed  
103 values along the conjuncted edge are represented by  $q_M^l$  and  $q_M^r$ .  $M$  is the  
104 middle point of the edge,  $N_{1-3}$  are the vertices of the left cell, cell averaged  
105 values of the left and right cells are represented by  $q_C$  and  $q_{D1}$ , respectively.  
106 Based on the work in [5],  $q_M^l$  can be extrapolated from the cell centroid based  
107 on a one-dimensional multislope MUSCL by

$$q_M^l = q_C + |\overrightarrow{CM}| \Psi(\nabla q_{N_3C}, \nabla q_{CM}), \quad (10)$$

108 where  $\overrightarrow{CM}$  is the vector from cell centroid  $C$  to edge middle point  $M$ , and  
109  $\nabla q_{N_3C}$  and  $\nabla q_{CM}$  represent the gradients from  $N_3$  to cell center and from  
110 the cell center to edge center, respectively.  $\Psi$  is the limiting function for re-  
111 stricting the reconstruction scheme to satisfy the total variation diminishing  
112 condition. The modified Van Albada's limiter with two arguments  $a$  and  $b$   
113 from [19] is adopted in this work,

$$\Psi(a, b) = \begin{cases} \frac{(a^2+e)b+(b^2+e)a}{a^2+b^2+2e} & \text{if } ab > 0 \\ 0 & \text{if } ab \leq 0 \end{cases} \quad (11)$$

114 Here,  $e = 10^{-12}$  used to avoid division by zero.

### 115 3.1. Vector manipulation methods

116 The two-dimensional multislope MUSCL schemes can be thought as a  
117 one-dimensional reconstruction process along the median line linking the cell  
118 center and the edge middle point, with the focus on the method for calcu-  
119 lating the upwind and downwind slopes of the cell center along the median



120 line. In the aforementioned literatures, slopes constructed by extrapolating  
 121 the upwind value along the cell centrelines [4, 9, 3], and the approximated  
 122 cell averaged method [20] have been studied. Owing to the accuracy and the  
 123 unphysical reconstruction point location at the edge, the multislope method  
 124 still needs to be further investigated.

125 Buffard and Clain [2] proposed the vector manipulation methods, where  
 126 upwind and downwind slopes can be calculated without the gradient calcula-  
 127 tion for the cells and the interpolation for the upwind points. Hou *et al.* [5]  
 128 simplified the original scheme to make the vector manipulation method more  
 129 straightforward to implement and enhance the robustness and accuracy.

130 As mentioned in [8], the main idea of the vector manipulation method  
 131 is to reconstruct the slopes from the cell centres to the slopes along the  
 132 line passing through the cell center and the edge middle point. It has been  
 133 shown that the methods from [2] and [5] include too much information from  
 134 the considered cells and may lead to a wrong reconstruction value along the  
 135 edge center. An improved vector manipulation method introduced in [8]  
 136 overcomes this disadvantage.

The legends are shown in Fig. 1, and the dimensional unit vector can be  
 calculated as,

$$\vec{r}_k = \frac{\overrightarrow{CN}_k}{|\overrightarrow{CN}_k|} \quad (12)$$

$$\vec{t}_k = \frac{\overrightarrow{CD}_k}{|\overrightarrow{CD}_k|}, \quad (13)$$

137 where  $\vec{r}_k$  and  $\vec{t}_k$  are the unit vectors from the considered cell center to the  
 138 vertices and the neighboring cell centres, respectively. It can be easily shown

139 that all the vector  $\vec{r}_k$  shall pass by the corresponding edge center along the  
 140 reverse direction.

141 The value slopes for the cell centres can be calculated along  $\vec{t}_k$  directions,

$$\nabla q_k = \frac{q_{D_k} - q_C}{|\overrightarrow{CD_k}|}. \quad (14)$$

142 The upwind and downwind slopes for the MUSCL reconstruction can be  
 143 thought as the slopes along the reverse direction of  $\vec{r}_k$  from the vertices to the  
 144 cell center and cell center to the edge center. For instance, the reconstructed  
 145 value  $q_M^l$  needs the slope along  $-\vec{r}_3$  and  $\overrightarrow{r_{CM}}$ , respectively.  $M$  represents the  
 146 middle of the edge.

In order to get the right information for the reconstruction, the unit vector  $\vec{r}_k$  is represented by the surrounding unit vector  $\vec{t}_k$ , with the consideration of geometric relationship obtained as

$$-\vec{r}_3 = \alpha_1 \vec{t}_2 + \alpha_2 \vec{t}_3 \quad (15)$$

$$\overrightarrow{r_{CM}} = \beta_1 \vec{t}_1 + \beta_2 \vec{t}_2. \quad (16)$$

Wherein, the coefficients  $\alpha_{1,2}$  and  $\beta_{1,2}$  can be solved by a set of linear equations. So that the upwind and downwind slopes can be computed as

$$\nabla q_{NC} = \alpha_1 \nabla q_2 + \alpha_2 \nabla q_3 \quad (17)$$

$$\nabla q_{CM} = \beta_1 \nabla q_1 + \beta_2 \nabla q_2. \quad (18)$$

147 In the work of Hou *et al.* [5],  $\nabla q_{NC}$  and  $\nabla q_{CM}$  are directly used as the  
 148 upwind and downwind slopes for the MUSCL reconstruction. An additional  
 149 step is added for obtaining more downwind information. From the geometric  
 150 relationship, it can be concluded that

$$\overrightarrow{r_{CM_k}} = \frac{|\overrightarrow{CD_k}|}{|\overrightarrow{CM_k}|} \overrightarrow{r_{CD_k}} + \frac{|\overrightarrow{D_k M_k}|}{|\overrightarrow{CM_k}|} \overrightarrow{r_{DM_k}}, \quad (19)$$

151 and then, Eq. 18 can be derived as

$$\nabla q_{CM_k} = \frac{|\overrightarrow{CD_k}|}{|\overrightarrow{CM_k}|} \nabla q_{CD_k} + \frac{|\overrightarrow{D_kM_k}|}{|\overrightarrow{CM_k}|} \nabla q_{D_kM_k}. \quad (20)$$

152 Here,  $k$  is the local index of the considered cell. This treatment has been  
 153 approved to give more physical reconstructed value and obtain good accuracy  
 154 in [8].

### 155 3.2. Improved vector manipulation method

156 As discussed in the previous section, including solely upwind information  
 157 decreases the stability of the scheme. The improved vector manipulation  
 158 scheme obtains more information from downwind direction. However, the  
 159 slope from cell centres to the edges centres  $\overrightarrow{r_{CM_k}}$  needs to be calculated  
 160 from the location relationships with the cell centres vectors  $\overrightarrow{t_k}$ . Additional  
 161 computational steps are needed to decide  $\overrightarrow{r_{CM_k}}$  located in which two cell  
 162 centres vectors  $\overrightarrow{t_k}$  before the calculation of Eq. 16, and the slope calculation  
 163 is highly influenced by the geometric distribution rather than the physical  
 164 values in VMM scheme. Therefore, an improved scheme is suggested here to  
 165 overcome the disadvantage of the previous schemes.

As shown in Fig. 2, all the vectors from the cell centers to the vertices

can be calculated as

$$\vec{r}_1 = \beta_{11} \vec{t}_1 + \beta_{12} \vec{t}_2 \quad (21)$$

$$\vec{r}_2 = \beta_{21} \vec{t}_1 + \beta_{22} \vec{t}_3 \quad (22)$$

$$\vec{r}_3 = \beta_{31} \vec{t}_2 + \beta_{32} \vec{t}_3 \quad (23)$$

$$\vec{r}_4 = \beta_{41} \vec{t}_4 + \beta_{42} \vec{t}_5 \quad (24)$$

$$\vec{r}_5 = \beta_{51} \vec{t}_4 + \beta_{52} \vec{t}_6 \quad (25)$$

$$\vec{r}_6 = \beta_{61} \vec{t}_5 + \beta_{62} \vec{t}_6 \quad (26)$$

166 and the relationship for the vectors can be easily derived as

$$\overrightarrow{DM} = \frac{\overrightarrow{DN}_1 + \overrightarrow{DN}_2}{2}, \quad (27)$$

167 considering the unit vectors  $r_k$ , Eq. 27 can be written into

$$\overrightarrow{r_{DM}} = \frac{|\overrightarrow{DN}_1|}{2|\overrightarrow{DM}|} \vec{r}_4 + \frac{|\overrightarrow{DN}_2|}{2|\overrightarrow{DM}|} \vec{r}_5, \quad (28)$$

so that, Eq. 16 can be changed to

$$\overrightarrow{r_{CM}} = \frac{|\overrightarrow{CD}|}{|\overrightarrow{CM}|} \vec{t}_1 + \frac{|\overrightarrow{DM}|}{|\overrightarrow{CM}|} \left( \frac{|\overrightarrow{DN}_1|}{2|\overrightarrow{DM}|} \vec{r}_4 + \frac{|\overrightarrow{DN}_2|}{2|\overrightarrow{DM}|} \vec{r}_5 \right) \quad (29)$$

$$= \frac{|\overrightarrow{CD}|}{|\overrightarrow{CM}|} \vec{t}_1 + \frac{|\overrightarrow{DN}_1|}{2|\overrightarrow{CM}|} \vec{r}_4 + \frac{|\overrightarrow{DN}_2|}{2|\overrightarrow{CM}|} \vec{r}_5 \quad (30)$$

$$= \frac{|\overrightarrow{CD}|}{|\overrightarrow{CM}|} \vec{t}_1 + \frac{|\overrightarrow{DN}_1|}{2|\overrightarrow{CM}|} (\beta_{41} \vec{t}_4 + \beta_{42} \vec{t}_5) + \frac{|\overrightarrow{DN}_2|}{2|\overrightarrow{CM}|} (\beta_{51} \vec{t}_4 + \beta_{52} \vec{t}_6), \quad (31)$$

the slope of cell centres are introduced, and then the downwind slope can be computed as

$$\begin{aligned} \nabla q_{CM} &= \frac{|\overrightarrow{CD}|}{|\overrightarrow{CM}|} \nabla q_{CD} + \frac{|\overrightarrow{DN}_1|}{2|\overrightarrow{CM}|} (\beta_{41} \nabla q_{DC} + \beta_{42} \nabla q_{DG}) \\ &\quad + \frac{|\overrightarrow{DN}_2|}{2|\overrightarrow{CM}|} (\beta_{51} \nabla q_{DC} + \beta_{52} \nabla q_{DE}). \end{aligned} \quad (32)$$

168 A local extrema violates the monotonicity principle [21]. The maximum  
 169 principle states that the extrapolated value along the edge midpoints of the  
 170 cell nodes can not be beyond the range of the local maximum and minimum  
 171 value. It is originally proposed in [22] to avoid over- and undershooting when  
 172 reconstructing the slopes for multi-dimensional problems on unstructured  
 173 grids. For the one-dimensional problem, the maximum principle can be used  
 174 as:

$$\mathbf{min}(q_l, q_r) \leq q_M^l, q_M^r \leq \mathbf{max}(q_l, q_r). \quad (33)$$

175 For the multi-dimensional problems, the reconstruction processes should try  
 176 to include more multi-dimensional flow physics [23]. The proposed MUSCL  
 177 reconstruction here includes 6 cells in the computational stencils. As shown  
 178 in Fig. 3, the schemes from Buffard and Clain [2] and Hou *et al.* [5] are  
 179 based on 4 cells, while the improved vector manipulation method from Zhao  
 180 *et al.* [8] is based on 5 cells. The vector manipulation methods satisfy the  
 181 maximum principle. It is hard to say whether more cells will lead to higher  
 182 accuracy, but the more information is included, the maximum principle will  
 183 be extended to a bigger range for the stability conditions, the less sensitive  
 184 to local mesh distribution and faithfully represents multi-dimensional flow  
 185 physics [23]. However, we shall note that the benefit of adding more cells to  
 186 the stencil can be expected to diminish after a certain number.

187 The aim of MUSCL reconstruction is to give values at the left and right  
 188 cell interface that can be used to construct a Riemann problem and calculate  
 189 the slope source term. The solution of the Riemann problem then yields the  
 190 numerical flux in Eq. (6) [16] and the slope source will be added into the  
 191 fluxes across the edge. In this work, a Harten, Lax and van Leer Riemann

192 solver with the contact wave restored (HLLC) [24] is used. The positivity  
 193 preserving hydrostatic reconstruction by [25] is used to maintain non-negative  
 194 water depth and correct reconstruction of the Riemann states, and the C-  
 195 property preserving divergence form of the bed slope source term proposed  
 196 by Hou *et al.* [26] is used; the source term treatment does not influence the  
 197 well-balanced property of the MUSCL schemes.

198 For the friction source term, the most straightforward technique is explicit  
 199 in time. However, this approach yields numerical instabilities unless the time  
 200 step size  $\Delta t$  satisfies [27]:

$$-1 \leq 1 + \frac{\mathbf{s}(\mathbf{q}_i^{n+1,x})}{\mathbf{q}_i^{n+1,x}} \Delta t \leq 1, \quad (34)$$

where  $\mathbf{q}_i^{n+1,x}$  is the solution after adding the fluxes terms, and the time step  
 has to be calculated using

$$\Delta t_s = \text{Min}_{i=1,\dots,N} \left[ -2 \frac{\mathbf{q}_i^{n+1,x}}{\mathbf{s}(\mathbf{q}_i^{n+1,x})} \right] \quad (35)$$

$$\Delta t = \text{Min}(\Delta t_c, \Delta t_s), \quad (36)$$

201 where  $\Delta t$ ,  $\Delta t_s$  and  $\Delta t_c$  are time steps for the system, source term part and  
 202 conservation part, respectively. Depending on the source term, this might  
 203 result in a severe degradation of the time step size.

204 To overcome this limitation, in literature, e.g. [26, 12], the splitting point-  
 205 implicit method is adopted. This avoids the instability of the numerical  
 206 scheme for very shallow water depths.

207 In splitting point implicit methods, conserved variables inside the cell are  
 208 updated as

$$\mathbf{q}^{n+1} = \mathbf{q}^n + \frac{1}{\text{PI}} \left( -\frac{\Delta t}{A} \sum_k \mathbf{f}_k^n \cdot \mathbf{n}_k l_k + \Delta t \mathbf{s}^n \right), \quad (37)$$

209 here,  $n$  and  $n + 1$  represent the time levels and  $\mathbf{PI}$  is a matrix equal to

$$\mathbf{PI} = \mathbf{I} - \Delta t \left( \frac{\partial \mathbf{s}}{\partial \mathbf{q}} \right)^n. \quad (38)$$

210 The momentum friction source terms are derived with respect to the unit  
 211 discharge, except the slope source term that has been transformed into fluxes  
 212 over the cell edges. Eq. 38 then yields

$$\mathbf{PI} = [1 - \Delta t(\partial s_x / \partial q_x)^n, 1 - \Delta t(\partial s_y / \partial q_y)^n]^T. \quad (39)$$

213 This gives

$$\frac{\partial s_x}{\partial q_x} = -\frac{c_f}{h^2} \left( \hat{q} + \frac{q_x^2}{\hat{q}} \right), \quad (40)$$

214

$$\frac{\partial s_y}{\partial q_y} = -\frac{c_f}{h^2} \left( \hat{q} + \frac{q_y^2}{\hat{q}} \right), \quad (41)$$

215 where  $\hat{q} = \sqrt{q_x^2 + q_y^2}$  is the magnitude of the unit discharge vector.

216 In order to preserve the stability, the general treatment from [21] is  
 217 adopted here, which locally switches the second order MUSCL scheme to  
 218 first order in a cell when the flow condition satisfying:

$$h_M^L \leq \mathbf{min}(|z_{bM}^L - z_c|, 0.25h_c) \text{ or } h_c \leq \epsilon_{wd} \quad (42)$$

219 here,  $h_M^L$  and  $z_M^L$  represent the reconstructed water depth and bottom eleva-  
 220 tion, respectively, along the considered edge;  $h_c$  and  $z_c$  are the corresponding  
 221 values at the cell center,  $\epsilon_{wd}$  is the tolerance used to distinguish the wet and  
 222 dry cells, which is set to  $\epsilon_{wd} = 10^{-6}$  in this study.

223 The procedures of MUSCL reconstruction methods for vector manipula-  
 224 tion method (VMM) and the improved vector manipulation method (IVMM)  
 225 are summarized in Table 1.

## 226 4. Numerical Tests

227 Five computational test cases published in the literature are presented  
228 here for verifying the MUSCL reconstruction methods. The performance of  
229 MUSCL reconstruction methods will be evaluated in terms of accuracy and  
230 efficiency. Two types of meshes, namely the diagonal mesh and the Delaunay  
231 mesh, are considered in evaluating each MUSCL reconstruction, as seen in  
232 Fig. 4.

233 The first test case considers a Riemann problem from Toro [28] as a  
234 benchmark to verify the stability and the efficiency of the MUSCL schemes.  
235 Moving shorelines in a two-dimensional frictional parabolic bowl is chosen as  
236 the second test case, where the proposed MUSCL schemes are verified for the  
237 accuracy and the capability to deal with wet and dry interface. Meanwhile,  
238 the performance of the friction source term treatment, and the grid conver-  
239 gence performance are investigated based on this test. The third and the  
240 forth examples are the MUSCL schemes are tested against the dam-break  
241 in a 45° channel and a two-dimensional dam-break flow against an isolated  
242 obstacle for evaluating how the MUSCL schemes perform on complex geom-  
243 etry for shock wave capturing. The final test cases are the near real-world  
244 application for the Malpasset dam-break. The accuracy is reflected by the  
245  $L_1$ -error which can be calculated as

$$L_1 = \frac{\sum_1^n |q_i - q_{i,\text{ref}}| A_i}{\sum_1^n A_i}, \quad (43)$$

246 which  $q_i$  and  $q_{i,\text{ref}}$  are the numerical solution and the reference solution in  
247 cell  $i$ , respectively. A characteristic length  $\Delta x = \sqrt{A/N}$  is used here for the  
248 resolution of the meshes,  $A$  and  $N$  are the total area and the number of cells.



249 *4.1. Dam break problems*

250 Two challenging problems proposed by Toro [28] are used here for examin-  
251 ing the capability to resolve the linear and non-linear waves on unstructured  
252 grids. A frictionless rectangular channel with  $[0, 50] \times [0, 0.25]$  m is discretized  
253 into 12032 Delaunay triangular meshes. Initial conditions of the test cases  
254 are summarized in Tab. 2, where  $h_L$ ,  $h_R$ ,  $u_L$  and  $u_R$  donates the initial water  
255 depth and the velocity in the left and right hand side of the discontinuity,  $x_0$   
256 is the location of the discontinuity,  $t_{out}$  is the output time.

257 Different initial conditions lead to different results after a short period,  
258 which the configuration *a* leads to a result with the left wave as a rarefaction  
259 wave transport to the left and the right wave as a shock transport to the  
260 right. Configuration *b* generate a two rarefaction wave transport to a opposite  
261 direction, in the middle of the computational domain, a very shallow water  
262 depth keeps a constant value. The results are compared considering the  
263 water elevation  $h$  and hydraulic head calculated via  $e = h + \frac{U^2}{2g}$ . The exact  
264 solution (—), numerical solutions from VMM (— \* —) and IVMM (— o —)  
265 are shown in Fig. 5, it can be observed that the numerical results are quite  
266 coincide with the exact solution from Toro [28], there is a little diffusion at  
267 the front of the waves, the VMM and IVMM provide the same quality results.  
268 The comparisons of the computational efficiency are based on the averaged  
269 computational time for a single step  $\Delta t$ , which is calculated by  $\Delta t = t_{total}/n$ ,  
270 where  $t_{total}$  is the total computational time and  $n$  is the number of time steps  
271 for the calculation. Each  $\Delta t$  in VMM is bigger than in IVMM for 3.6%, 2.9%  
272 in configuration *a* and *b*, respectively. This means that IVMM can obtain a  
273 better efficiency than VMM scheme. The result is as expected in the previous

274 section, the additional step used for searching the vectors  $t$  will increase the  
 275 computational time and decrease the computational efficiency.

276 *4.2. Moving shorelines in a two-dimensional frictional parabolic bowl*

277 The analytical solution of the moving shorelines in a two-dimensional  
 278 frictional parabolic bowl was developed by Sampson *et al.* [29], it will be  
 279 used to validate the proposed model for the MUSCL reconstruction and  
 280 frictional treatment here. The bed topography is described as,

$$z(x, y) = h_0[(x - x_0)^2 + (y - y_0)^2]/a^2. \quad (44)$$

Here,  $z(x, y)$  represent the bottom elevation of the  $(x, y)$  point,  $x_0, y_0$  is the coordinate of the geometry center.  $h_0$  is the initial water depth at the parabola center, and  $a$  is a constant value.  $\tau$  is the bed frictional parameter, and  $c_f = h\tau/\sqrt{u^2 + v^2}$ . The peak amplitude parameter  $p = \sqrt{8gh_0}/a$ , if  $\tau < p$ , the analytical solution for the water level is given by

$$\begin{aligned} \eta(x, y, t) = h_0 - \frac{B^2 e^{-\tau t}}{2g} - \frac{B e^{-\tau t/2}}{g} \left\{ \left[ \frac{\tau \sin(st)}{2} + s \cos(st) \right] (x - x_0) \right. \\ \left. + \left[ \frac{\tau \cos(st)}{2} - s \sin(st) \right] (y - y_0) \right\}, \end{aligned} \quad (45)$$

and the analytical solution for the velocities are

$$u(t) = B e^{-\tau t/2} \sin(st) \quad (46)$$

$$v(t) = B e^{-\tau t/2} \cos(st), \quad (47)$$

281 where  $B$  is a constant as an initial value of  $v(0)$ , and  $s = \sqrt{p^2 - \tau^2}/2$ , in  
 282 which  $p = \sqrt{8gh_0}/a$ .

283 A square computational domain of  $8000 \times 8000$  m with the center at  
 284  $(0.0, 0.0)$  is chosen as the study area. The parameters are set to  $h_0 = 10$  m,

285  $a = 3000$ ,  $B = 5$  m/s and  $\tau = 0.002$  s<sup>-1</sup>. The computational domain is  
 286 discretized with two types of meshes with 5 refinement levels for the mesh  
 287 convergence. The boundaries are all set to closed boundaries, and the sim-  
 288 ulation time runs until  $t = 6000$  s, which is almost 4 periods. The initial  
 289 condition can be obtained from Eqs. 45 - 47.

290 The contours plot at  $t = 1500$  s, which is almost 1.1 period after the  
 291 simulation begin can be seen in Fig. 6. The difference between VMM and  
 292 IVMM scheme results is quite small, both of the schemes can capture the  
 293 water depth quite well at diagonal grid and Delaunay grid at the first mesh  
 294 level. The cut section plot along the diagonal line of the computational  
 295 domain at  $t = 500$  s and  $t = 1500$  s are shown in Fig. 7 and Fig. 8 for the  
 296 Delaunay and diagonal grids, respectively. In order to show the accuracy of  
 297 the MUSCL reconstruction, the results at the first mesh level (finest mesh)  
 298 and the fifth mesh level (coarsest mesh) are chosen for the comparison. The  
 299 water level ( $wl$ ) and the discharge along  $x$ - direction ( $q_x$ ) and  $y$ - direction  
 300 ( $q_y$ ) are all captured well with the analytical solution at the finest mesh; for  
 301 the coarsest mesh, water levels  $wl$  are captured well for both grids types,  
 302 but for the discharges, it can be observed that the results of diagonal grids  
 303 agree worse than that of Delaunay grids, especially for  $q_x$ , and the result  
 304 from IVMM is slightly better than the VMM scheme.

305 A mesh convergence study for this test case at  $t = 1500$  s is presented  
 306 in Fig. 9. The  $L_1$  errors for  $h$  and  $q_y$  are plotted in the figures for the  
 307 different mesh level (represented by the characteristic length  $\Delta x$  shown in  
 308 Tab. 3). The results from VMM and IVMM are represented by the  $\circ - \circ$  and  
 309  $\triangleright - \triangleright$ , respectively. It can be seen that the order of VMM and IVMM are all

310 slightly lower than the slope 2 (solid lines). This is because of the wet and  
311 dry interfaces, where the order of the scheme will switch to first order, which  
312 decreases the overall order of accuracy. The VMM and IVMM schemes are  
313 nearly parallel with the increasing of the mesh level, but the error values for  
314 the IVMM scheme is almost always smaller than the corresponding error for  
315 the VMM scheme, which can be thought the order of the IVMM scheme and  
316 VMM scheme is similar but the accuracy of the IVMM scheme is better. As  
317 the characteristic length  $\Delta x$  is different for the Delaunay and diagonal grids,  
318 the errors for the diagonal grids is a little bit higher than for the Delaunay  
319 grids. It was already shown the diagonal grids will significantly influence the  
320 results for the MUSCL reconstructions in [8], it can be observed here that  
321 the  $q_y$  for the VMM scheme leads to higher error compared to the results  
322 from IVMM scheme, which means the IVMM is less influenced from the grid  
323 type.

324 The relative time of VMM against IVMM scheme is shown in Fig. 10. It  
325 can be clearly observed that IVMM provides a relatively better efficiency than  
326 VMM scheme, and with the increasing of the mesh number, the advantage  
327 becomes bigger. The unstructured grids in this work are mainly focused on  
328 the triangle mesh, where the vector structure in the single cell is still simple,  
329 but for a more complex mesh, the additional calculation will increase, which  
330 will decrease the computational efficiency even more.

#### 331 4.3. Dam-break in a channel with $45^\circ$ bend

332 To assess the performance of the MUSCL reconstructions for the dam-  
333 break induced waves in non-straight channels, a test case from EU CADAM  
334 [30] is chosen as the benchmark, which was also considered in [12, 31, 32] for

335 verifying the capability of their model for dam-break simulation. The set up  
336 and the computational grid used for the simulation of the experiment facility  
337 can be seen in Fig. 11. The reservoir with the size  $2.39 \times 2.44 \text{ m}^2$  is located at  
338 the left side of the experiment, the northwest of the reservoir is set to be the  
339 origin position of the geometry, a 0.495 m wide channel with a  $45^\circ$  bending  
340 corner is connected with the reservoir and with a free outlet for the end of  
341 the channel. The water depth for the reservoir and the channel are 0.58 m  
342 and 0 m, respectively. A 0.33 m high topography step is located between  
343 the reservoir and the channel. The Manning number is suggested equal  
344 to  $0.012 \text{ s/m}^{1/3}$  after the preliminary numerical tests. The computational  
345 domain is discretized into 13038 Delaunay triangles-based meshes.

346 The simulation results from VMM and IVMM scheme are compared with  
347 the measurement data for three gauges located as shown in Tab. 4. As  
348 shown in Fig. 12, after 40 s, the water elevation is quite well predicted by  
349 the numerical results, the only overestimated water elevation is after 5s at  
350 G6 and underestimated after 20s at G9, which may come from the three  
351 dimensional effects after the  $45^\circ$  bend. It also can be observed that the  
352 difference between the IVMM and VMM scheme is quite small, they all  
353 provide promising result, but again, the IVMM is about 4.1% faster than  
354 the VMM scheme, which indicates that the proposed scheme is sufficient for  
355 simulating the dam-break flow over dry bed even discontinuity.

#### 356 4.4. *Two-dimensional dam-break flow against an isolated obstacle*

357 A physical experiment is set up for two-dimensional dam-break flow against  
358 an isolated obstacle constructed by Soares-Frazão and Zech [33]. It is chosen  
359 for testing the capability of the MUSCL reconstructions work on asymmet-

360 ric geometry, the water elevation and the velocity will be checked for both  
361 numerical schemes. The sketch of the experiment is shown in Fig. 13, with a  
362 trapezoidal bottom for the up and downstream channel and the cut sections  
363 can be found in Fig. 13, all the boundaries are closed except for the channel  
364 outlet. The initial water level for the reservoir and down stream of the dam  
365 are 0.4 m and 0.02 m, respectively. The dam-break is simulated by removing  
366 the gate in a sudden period. The velocities and water levels are measured  
367 in the different gauges located in the positions shown in Tab. 5, and the  
368 coordinate origin is set at the center of the gate.

369 The computational domain is discretized into 27831 triangle cells, rela-  
370 tively coarse mesh in the reservoir and a higher resolution for the downstream  
371 of the dam. The velocity field is set to be still for the beginning of the simu-  
372 lation. Numerical test will run for 30 s and the Manning coefficient is chosen  
373  $n = 0.01 \text{ s/m}^{1/3}$  by following [33].

374 After 30 s, the simulation results from VMM and IVMM compared with  
375 the measurement data are shown in Fig. 15, the water elevation is shown in  
376 the left column. It can be observed that the measured data is fairly good  
377 predicted by the numerical results, both MUSCL reconstructions show good  
378 agreement, but IVMM shows a little bit better results at gauge G2, however,  
379 the VMM is slightly better at G1. However, the IVMM leads to more stable  
380 results. The middle column presents the velocity along the  $x$ - direction, the  
381 measurement data agrees well with the numerical results except for the G1,  
382 this maybe caused by the strong three dimensional effects near the obstacle.  
383 The VMM shows a slightly faster wave front at G5, here VMM may give a  
384 better prediction because of the faster wave speed, but it is difficult to say

385 which one is better. The right column shows the velocity along the  $y$ - direc-  
386 tion, it can be observed that the range of the velocity value is smaller than  
387 the measurement data, as the obstacle provides a three dimensional influence  
388 on the flow field, which is neglected by the shallow water model. However,  
389 the water level at G6 seen in Fig. 16, shows that the numerical results per-  
390 fectly captured the measured data, which means that both of the schemes  
391 can capture the long wave well. Again, the single computational effort is  
392 compared, and the IVMM can save 9.51% computational time compared to  
393 the IVMM scheme.

#### 394 *4.5. Malpasset dam-break*

395 The last example is chosen to be the Malpasset dam-break for test the  
396 capability of the numerical model for simulating the field scale case. The  
397 Malpasset dam is located on the Reyran River valley and the associated  
398 floodplain in southern France is shown as in Fig. 17 (a). The topography  
399 is provided by [34] and the computational domain is discretized into 28855  
400 triangle cells as shown in Fig. 17 (b) and the boundaries are set to be  
401 solid walls except for the downstream boundaries near to the sea which is  
402 transmissive. The reservoir has a constant water level for 100 m above the  
403 sea level, and the downstream of the dam is set to be initially dry except for  
404 the sea. The Manning coefficient is set to  $0.033 \text{ s/m}^{1/3}$ , following [35, 5, 26,  
405 34, 36, 12].

406 Laboratory studies were carried out by Electricité de France to measure  
407 the arrival time and the maximum water level at the gauge points G (6-  
408 14) and the police points P (1-17), the measurement data is well matched  
409 with the field data, and will be used for validating the numerical schemes.

410 Simulation runs until 3600s and the water depth floodplain simulated by  
411 IVMM scheme is shown as in Fig. 18.

412 After 3600 s, the arriving time at the electrical transformers is compared  
413 in Fig. 19(a), which the IVMM scheme reaches a little faster than the VMM  
414 scheme, being closer to the measurement data. The summary of the max-  
415 imum water level of the survey points is shown in Fig. 19(b), it can be  
416 observed that the simulated results from both MUSCL schemes show fairly  
417 well agreement with the measurement data. Small discrepancies happen at  
418 the experiment gauges for the arriving time of the water, this can be due  
419 to the limitation of the two-dimensional SWEs and certain complex flows  
420 with three-dimensional effects will also influence the measurement results.  
421 This simulated results also well match the results from the literature, e.g.  
422 [5, 26, 12]. However, in general, the simulated results provided by VMM  
423 and IVMM can well predict the field measurements, there is no negative  
424 water depth predicted, nor are non-physical velocities created by the pro-  
425 posed schemes. To the end, the computational efficiency is compared and  
426 the IVMM saves 10.5% computation time compared to the VMM scheme.

## 427 5. Conclusions

428 An improved vector manipulation of the multislope MUSCL method is  
429 proposed in this work to achieve high accuracy and efficiency for the two-  
430 dimensional unstructured cell-centered finite volume modelling of shallow  
431 water flows. The proposed scheme is proven to be more straight-forward  
432 without including any additional step for judging the geometry relationships.  
433 Five examples involving analytical solution, laboratory experiments and field-



434 scale surveys are used for validating the proposed scheme, and all the results  
435 are compared with those of the original vector manipulation method from  
436 [8]. The results from the proposed MUSCL reconstruction are shown to pro-  
437 duce satisfactory results without creating negative water depth and infinite  
438 velocity. The mesh convergence study shows that the new scheme is roughly  
439 second order accuracy. The computational cost is compared in each test  
440 case, the new IVMM scheme is shown to save about 4%-10% computational  
441 time compared to the VMM scheme, and the saving is more apparent with  
442 more computational grid points. To sum up, the new reconstruction method  
443 exhibits good performance for solving the SWEs on unstructured grids.

#### 444 **Acknowledgements**

445 The authors are grateful to the China Scholarship Council and TU Berlin  
446 for the scholarships granted to J. Zhao.

447 [1] B. van Leer, Towards the ultimate conservative difference scheme. V.  
448 A second-order sequel to Godunov's method, *Journal of Computational*  
449 *Physics* 32 (1979) 101–136.

450 [2] T. Buffard, S. Clain, Monoslope and multislope MUSCL methods for un-  
451 structured meshes, *Journal of Computational Physics* 229 (2010) 3745–  
452 3776.

453 [3] M. Darwish, F. Moukalled, TVD schemes for unstructured grids, *Inter-*  
454 *national Journal of Heat and Mass Transfer* 46 (2003) 599–611.

- 455 [4] J. Hou, F. Simons, R. Hinkelmann, Improved total variation diminish-  
456 ing schemes for advection simulation on arbitrary grids, *International*  
457 *Journal for Numerical Methods in Fluids* 70 (2012) 359–382.
- 458 [5] J. Hou, Q. Liang, H. Zhang, R. Hinkelmann, Multislope MUSCL method  
459 applied to solve shallow water equations, *Computers & Mathematics*  
460 *with Applications* m (2014).
- 461 [6] S. K. Godunov, A difference method for numerical calculation of dis-  
462 continuous equations of hydrodynamics (in Russian), *Matematicheskii*  
463 *Sbornik* 47 (1959) 271–300.
- 464 [7] V. Venkatakrishnan, Convergence to Steady State Solutions of the Euler  
465 Equations on Unstructured Grids with Limiters, *Journal of Computa-*  
466 *tional Physics* 118 (1995) 120–130.
- 467 [8] J. Zhao, I. Özgen, D. Liang, R. Hinkelmann, Improved multislope muscl  
468 reconstruction on unstructured grids for shallow water equations, *Inter-*  
469 *national Journal for Numerical Methods in Fluids* 0 (2018) 1–36.
- 470 [9] X. Li, H. Liao, An improved r-factor algorithm for TVD schemes, *In-*  
471 *ternational Journal of Heat and Mass Transfer* 51 (2008) 610–617.
- 472 [10] Q. Liang, A. G. Borthwick, Adaptive quadtree simulation of shallow  
473 flows with wetdry fronts over complex topography, *Computers & Fluids*  
474 38 (2009) 221–234.
- 475 [11] Q. Liang, F. Marche, Numerical resolution of well-balanced shallow wa-  
476 ter equations with complex source terms, *Advances in Water Resources*  
477 32 (2009) 873–884.

- 478 [12] J. Hou, F. Simons, M. Mahgoub, R. Hinkelmann, A robust well-balanced  
479 model on unstructured grids for shallow water flows with wetting and  
480 drying over complex topography, *Computer Methods in Applied Me-*  
481 *chanics and Engineering* 257 (2013) 126–149.
- 482 [13] F. Simons, T. Busse, J. Hou, I. Özgen, R. Hinkelmann, A model for over-  
483 land flow and associated processes within the Hydroinformatics Mod-  
484 elling System, *Journal of Hydroinformatics* (2014) 1–26.
- 485 [14] Q. Liang, F. Marche, Numerical resolution of well-balanced shallow wa-  
486 ter equations with complex source terms, *Advances in Water Resources*  
487 32 (2009) 873–884.
- 488 [15] Q. Liang, Flood Simulation Using a Well-Balanced Shallow Flow Model,  
489 *Journal of Hydraulic Engineering* 136 (2010) 669–675.
- 490 [16] E. F. Toro, *Riemann Solvers and Numerical Methods for Fluid Dynam-*  
491 *ics*, Springer-Verlag, Berlin Heidelberg, 3 edition, 2009.
- 492 [17] T. Buffard, S. Clain, Monoslope and multislope MUSCL methods for un-  
493 structured meshes, *Journal of Computational Physics* 229 (2010) 3745–  
494 3776.
- 495 [18] V. Guinot, C. Delenne, MUSCL schemes for the shallow water sensitivity  
496 equations with passive scalar transport, *Computers and Fluids* 59 (2012)  
497 11–30.
- 498 [19] A. Delis, I. Nikolos, A novel multidimensional solution reconstruction  
499 and edge-based limiting procedure for unstructured cell-centered finite

- 500 volumes with application to shallow water dynamics, *International Journal for Numerical Methods in Fluids* 71 (2013) 584–633.
- 501
- 502 [20] J. Hou, F. Simons, R. Hinkelmann, A new TVD method for advection  
503 simulation on 2D unstructured grids, *International Journal for Numerical  
504 Methods in Fluids* 71 (2013) 1260–1281.
- 505 [21] J. Hou, Q. Liang, H. Zhang, R. Hinkelmann, An efficient unstructured  
506 muscl scheme for solving the 2d shallow water equations, *Environmental  
507 Modelling & Software* 66 (2015) 131–152.
- 508 [22] X.-D. Liu, A maximum principle satisfying modification of triangle  
509 based adaptive stencils for the solution of scalar hyperbolic conserva-  
510 tion laws, *SIAM journal on numerical analysis* 30 (1993) 701–716.
- 511 [23] J. S. Park, S. H. Yoon, C. Kim, Multi-dimensional limiting process for  
512 hyperbolic conservation laws on unstructured grids, *Journal of Computa-  
513 tional Physics* 229 (2010) 788–812.
- 514 [24] E. F. Toro, M. Spruce, W. Speares, Restoration of the contact surface  
515 in the HLL-Riemann solver, *Shock Waves* 4 (1994) 25–34.
- 516 [25] E. Audusse, F. Bouchut, M.-O. Bristeau, R. Klein, B. Perthame, A Fast  
517 and Stable Well-Balanced Scheme with Hydrostatic Reconstruction for  
518 Shallow Water Flows, *SIAM Journal on Scientific Computing* 25 (2004)  
519 2050–2065.
- 520 [26] J. Hou, Q. Liang, F. Simons, R. Hinkelmann, A 2D well-balanced shal-  
521 low flow model for unstructured grids with novel slope source term treat-  
522 ment, *Advances in Water Resources* 52 (2013) 107–131.

- 523 [27] V. Guinot, Godunov-type Schemes: An introduction for engineers, El-  
524 sevier Science B.V., Amsterdam, The Netherlands, 1 edition, 2003.
- 525 [28] E. F. Toro, Shock-capturing Methods for Free-surface Shallow Flows,  
526 John Wiley & Sons, New York/Chichester, 2001.
- 527 [29] J. Sampson, A. Easton, M. Singh, Moving boundary shallow water flow  
528 above parabolic bottom topography, *Anziam Journal* 47 (2006) 373–387.
- 529 [30] M. Morris, Cadam concerted action on dambreak modelling, Report SR  
530 571 (2000).
- 531 [31] H.-M. Kao, T.-J. Chang, Numerical modeling of dambreak-induced flood  
532 and inundation using smoothed particle hydrodynamics, *Journal of hy-*  
533 *drology* 448 (2012) 232–244.
- 534 [32] J. G. Zhou, D. M. Causon, C. G. Mingham, D. M. Ingram, Numerical  
535 prediction of dam-break flows in general geometries with complex bed  
536 topography, *Journal of hydraulic engineering* 130 (2004) 332–340.
- 537 [33] S. Soares-Frazão, Y. Zech, Experimental study of dam-break flow  
538 against an isolated obstacle, *Journal of Hydraulic Research* 45 (2007)  
539 27–36.
- 540 [34] G. N., The Malpasset dam failure. An overview and test case definition,  
541 *Proceedings of CADAM Zaragoza meeting* (1999) 1–7.
- 542 [35] Y. Wang, Q. Liang, G. Kesserwani, J. W. Hall, A 2d shallow flow model  
543 for practical dam-break simulations, *Journal of Hydraulic Research* 49  
544 (2011) 307–316.

545 [36] A. Valiani, V. Caleffi, A. Zanni, Case study: Malpasset dam-break  
546 simulation using a two-dimensional finite volume method, Journal of  
547 Hydraulic Engineering 128 (2002) 460–472.

Table 1: Procedures of MUSCL schemes, choose Fig. 2 as legend

Steps	Vector Manipulation (VMM)	Method	Improved Vector Manipulation Method (IVMM)
1	Compute $\vec{r}_k$ and $\vec{t}_k$		Compute $\vec{r}_k$ and $\vec{t}_k$
2	Solve Eqs. (15 & 16 ) to get the coefficients $\alpha_1, \alpha_2, \beta_1$ and $\beta_2$ .		Solve Eqs. (21-26) to get $\beta_{1-6,1-2}$
3	Calculate $\nabla q_{C,(D,F,H)}$ and $\nabla q_{D,(C,E,G)}$ from Eq. (14)		Calculate $\nabla q_{C,(D,F,H)}$ and $\nabla q_{D,(C,E,G)}$ from Eq. (14)
4	Evaluate $\nabla q_{NC}$ and $\nabla q_{CM}$ from Eq. (17 & 18)		Evaluate $\nabla q_{NC}$ and $\nabla q_{CM}$ from Eq. (17 & 32)
5	Update $\nabla q_{CM}$ with Eq. (20)		Update $\nabla q_{CM}$ with Eq. (20)
6	Extrapolate the edge value by following Eq. (10)		Extrapolate the edge value by following Eq. (10)

Table 2: Initial conditions for Toro's test problems.

Test	$h_L$ (m)	$u_L$ (m/s)	$h_R$ (m)	$u_R$ (m/s)	$x_0$ (m)	$t_{out}$ (s)
a	1.0	2.5	0.1	0.0	10.0	7.0
b	1.0	-5.0	1.0	5.0	25.0	2.5

Table 3: Characteristic length  $\Delta x$  (m) used for the mesh convergence test

Mesh Level	Diagonal Mesh	Delaunay Mesh
1	35.355	30.708
2	52.868	45.967
3	70.711	61.612
4	88.386	77.110
5	104.752	91.630

Table 4: Position of measurement gauges.

Gauge	x [m]	y [m]
4	5.7400	0.6925
6	6.6488	0.7650
9	8.1267	2.2428



Table 5: Two-dimensional dam-break flow against an isolated obstacle: position of measurement gauges.

Gauge	x (m)	y (m)
G1	2.65	1.15
G2	2.65	-0.60
G3	4.00	1.15
G4	4.00	-0.80
G5	5.20	0.30
G6	-1.87	1.10

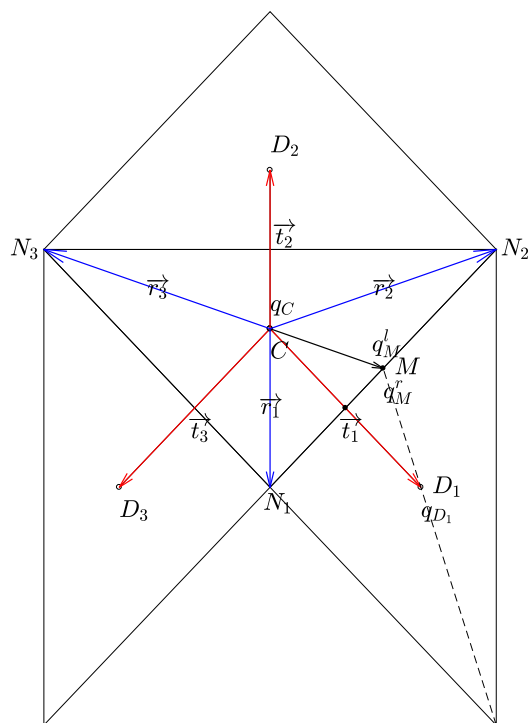


Figure 1: Definition of the considered cell and the neighbor cells.

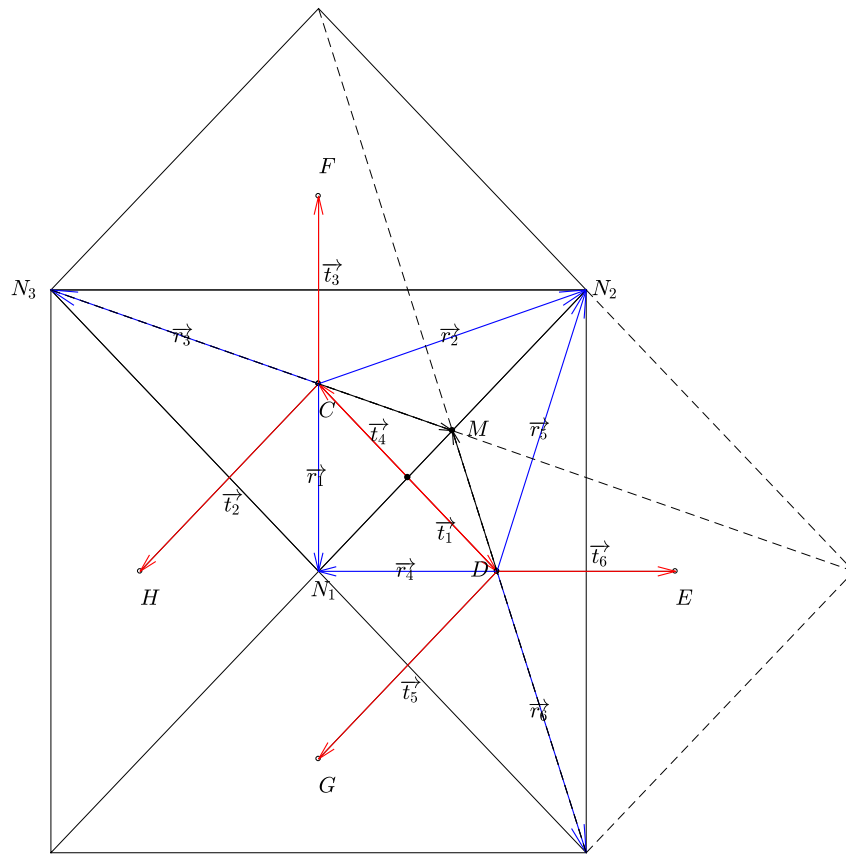


Figure 2: Stencils for new vector manipulation method.

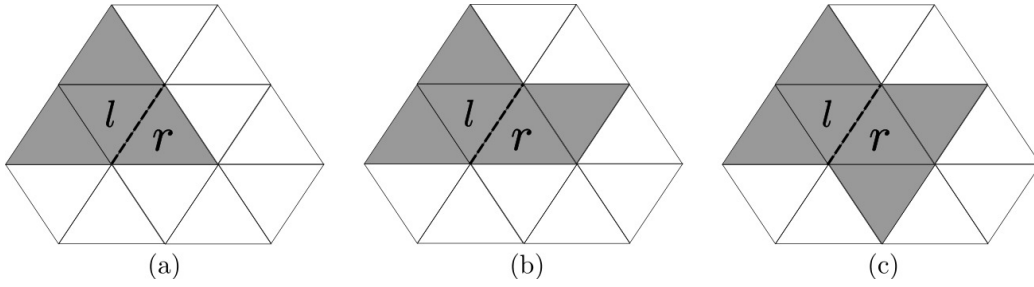


Figure 3: Comparison of stencils involved in limiting and the maximum principle. Shaded region is the stencil for the maximum principle, and the dotted line is the edge for limiting. (a) Limiter from Buffard and Clain [2] and Hou *et al.* [5], (b) limiter from Zhao *et al.* [8] and (c) new limiter in this work.

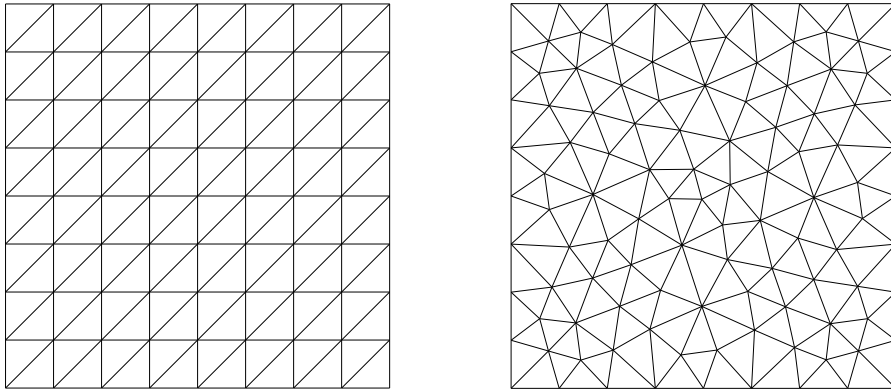


Figure 4: The two types of mesh employed to evaluate the accuracy and efficiency of the schemes: the diagonal mesh (left) and the Delaunay mesh (right)

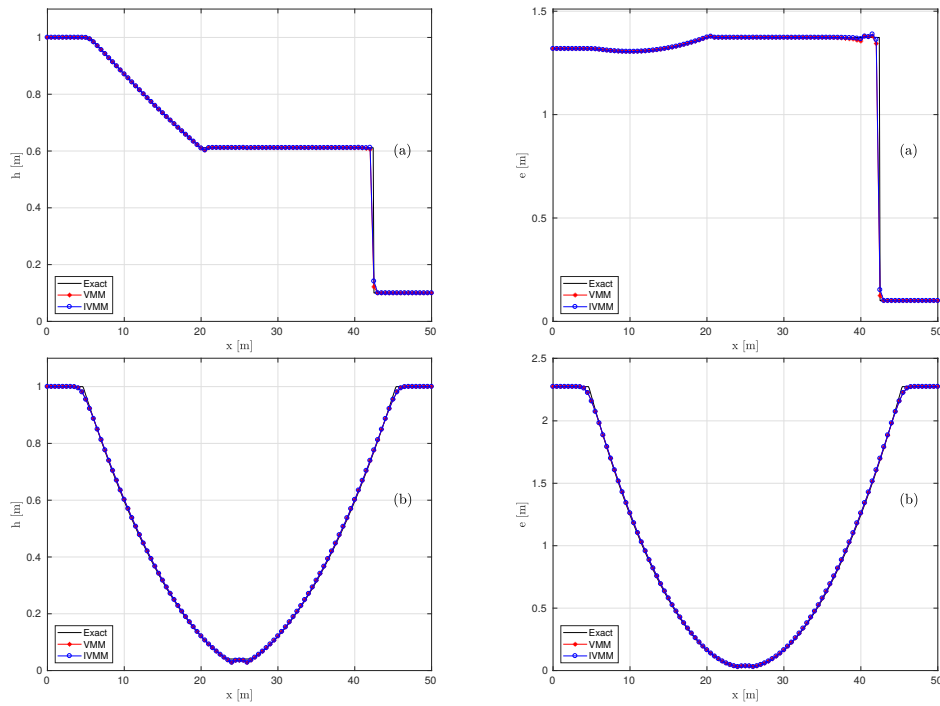


Figure 5: Comparison of numerical and exact solution for Toro's Riemann problems: left rarefaction wave and right shock wave: water elevation (a left), hydraulic head (a right); two rarefaction waves and nearly dry bed: water elevation (b left), hydraulic head (b right).

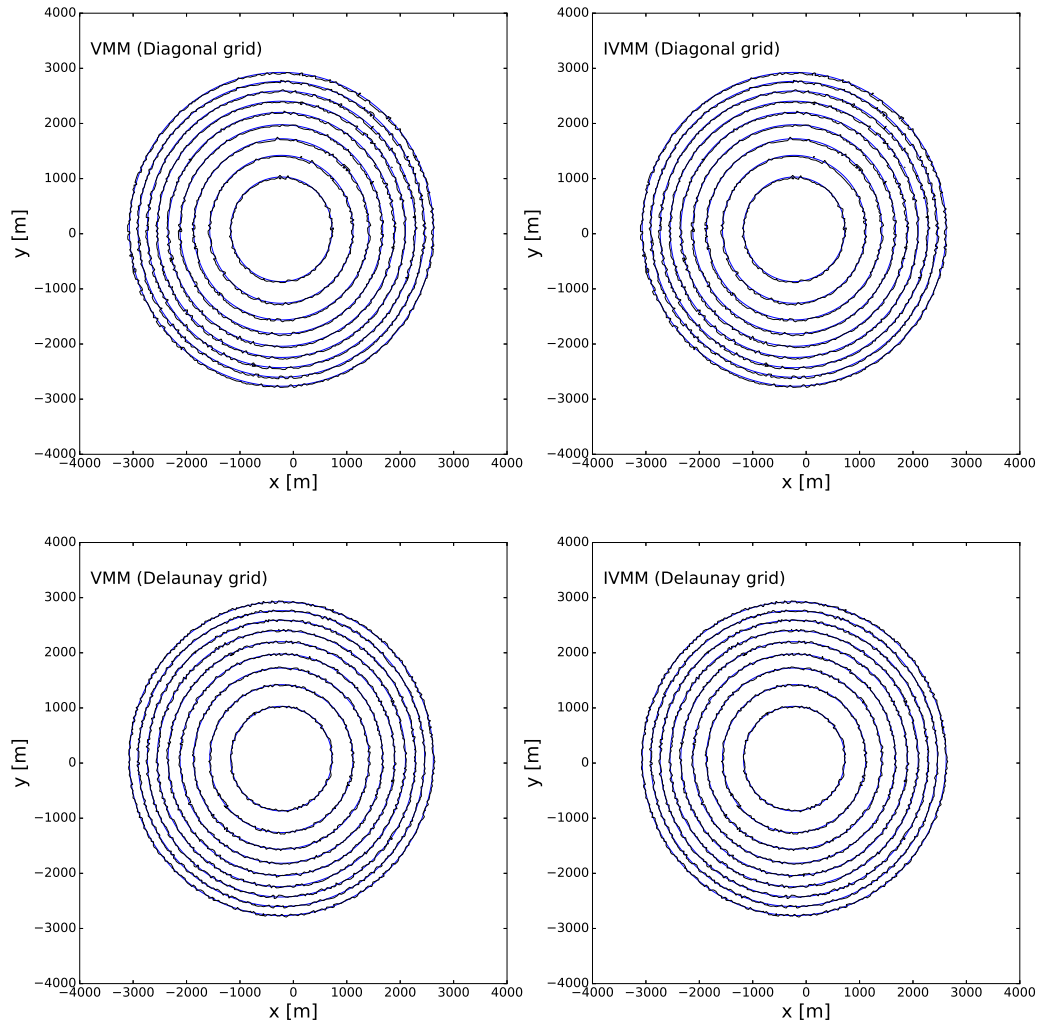


Figure 6: Moving shorelines in a two-dimensional frictional parabolic bowl: contours of water depth computed by VMM scheme (black lines located at the left side) and the result from IVMM scheme (black lines located at the right side) by using the diagonal grid (level 5, for the upper part) and the Delaunay grid (level 5, for the lower part) compared with the analytical solution (blue lines) at  $t = 1500$  s.

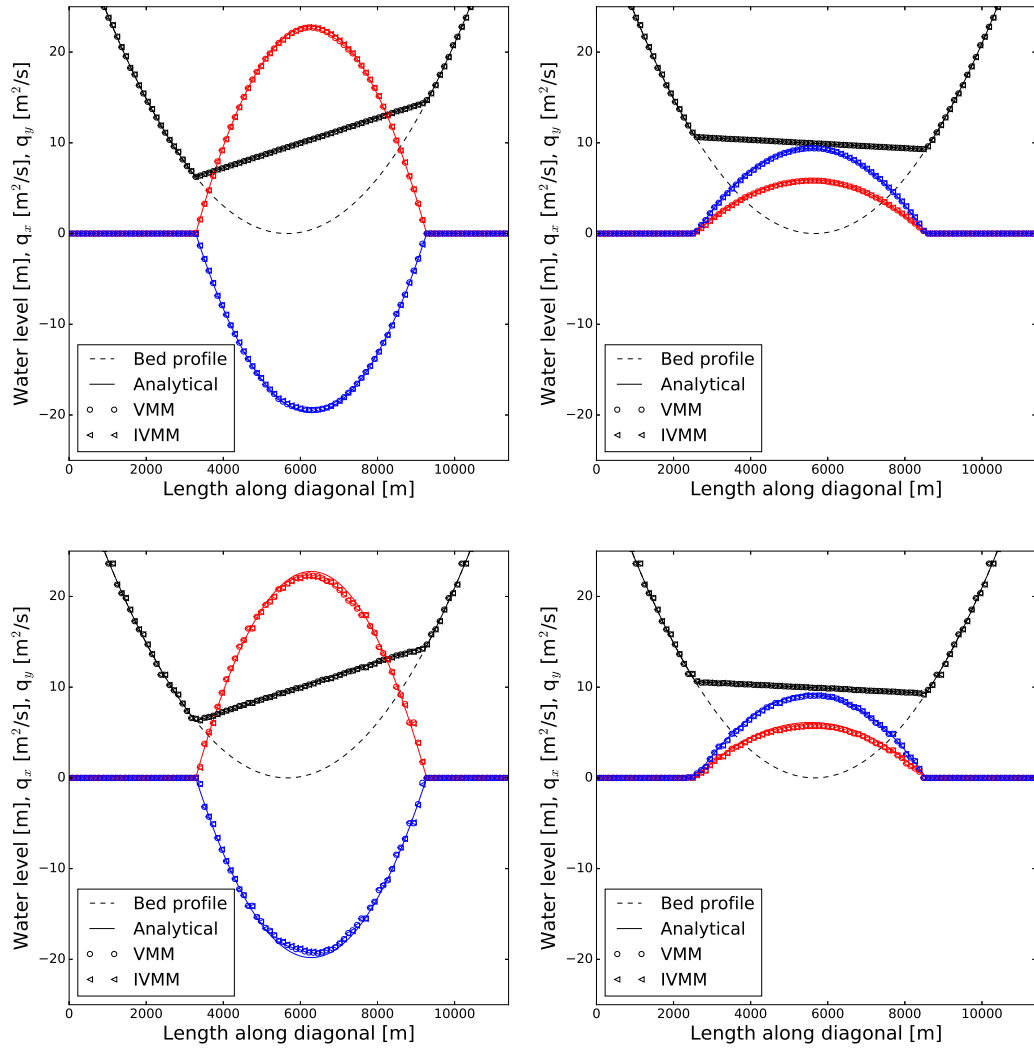


Figure 7: Moving shorelines in a two-dimensional frictional parabolic bowl: comparison between analytical solution (-) and the numerical solution (Delaunay mesh): VMM( $\circ \circ$ ), IVMM( $\triangleleft \triangleleft$ ) for the water level (black),  $q_x$  (red),  $q_y$  (blue) for  $t = 500$  s (left) and  $t = 1500$  s (right) for the Delaunay grid in level 1 (upper) and level 5 (lower).

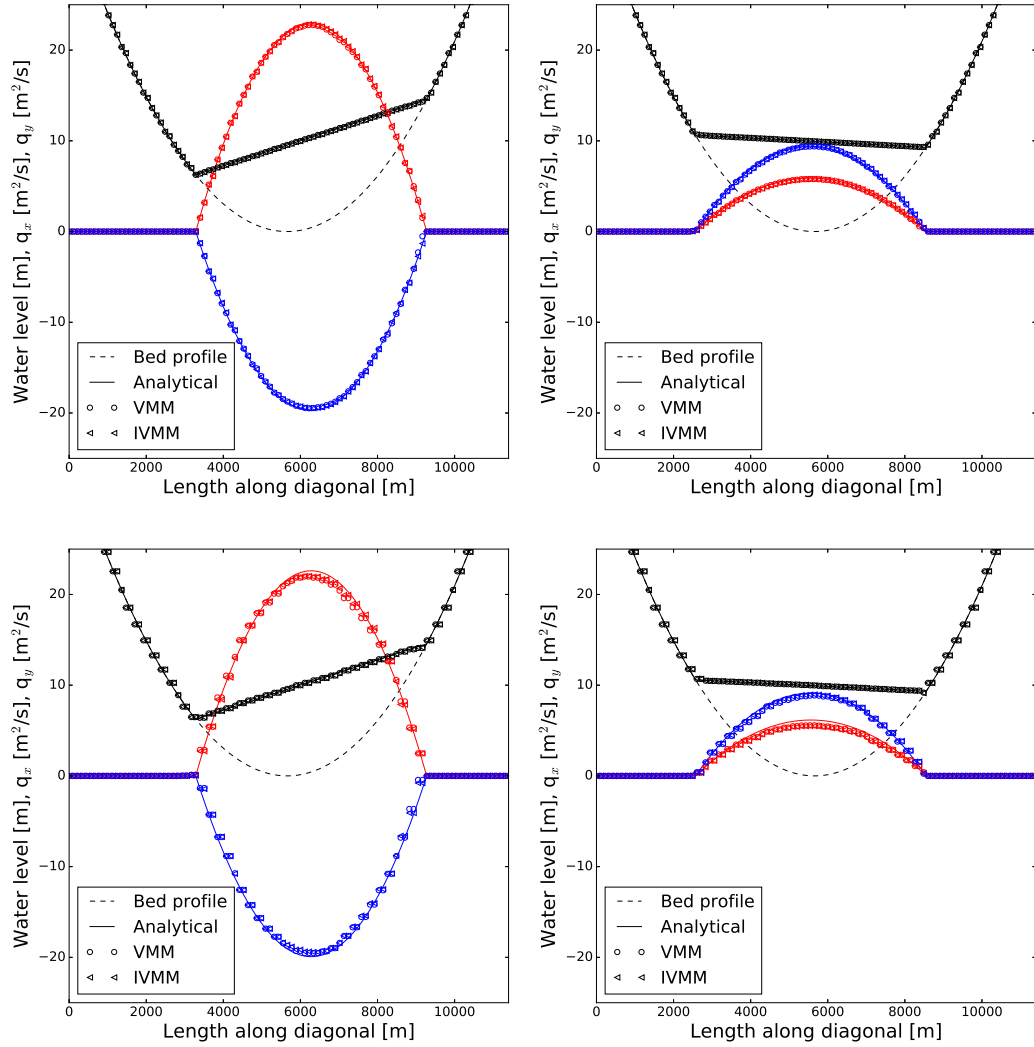


Figure 8: Moving shorelines in a two-dimensional frictional parabolic bowl: comparison between analytical solution (-) and the numerical solution (diagonal mesh): VMM( $\circ \circ$ ), IVMM( $\triangleleft \triangleleft$ ) for the water level (black),  $q_x$  (red),  $q_y$  (blue) for  $t = 500$  s (left) and  $t = 1500$  s (right) for the diagonal grid in level 1 (upper) and level 5 (lower).

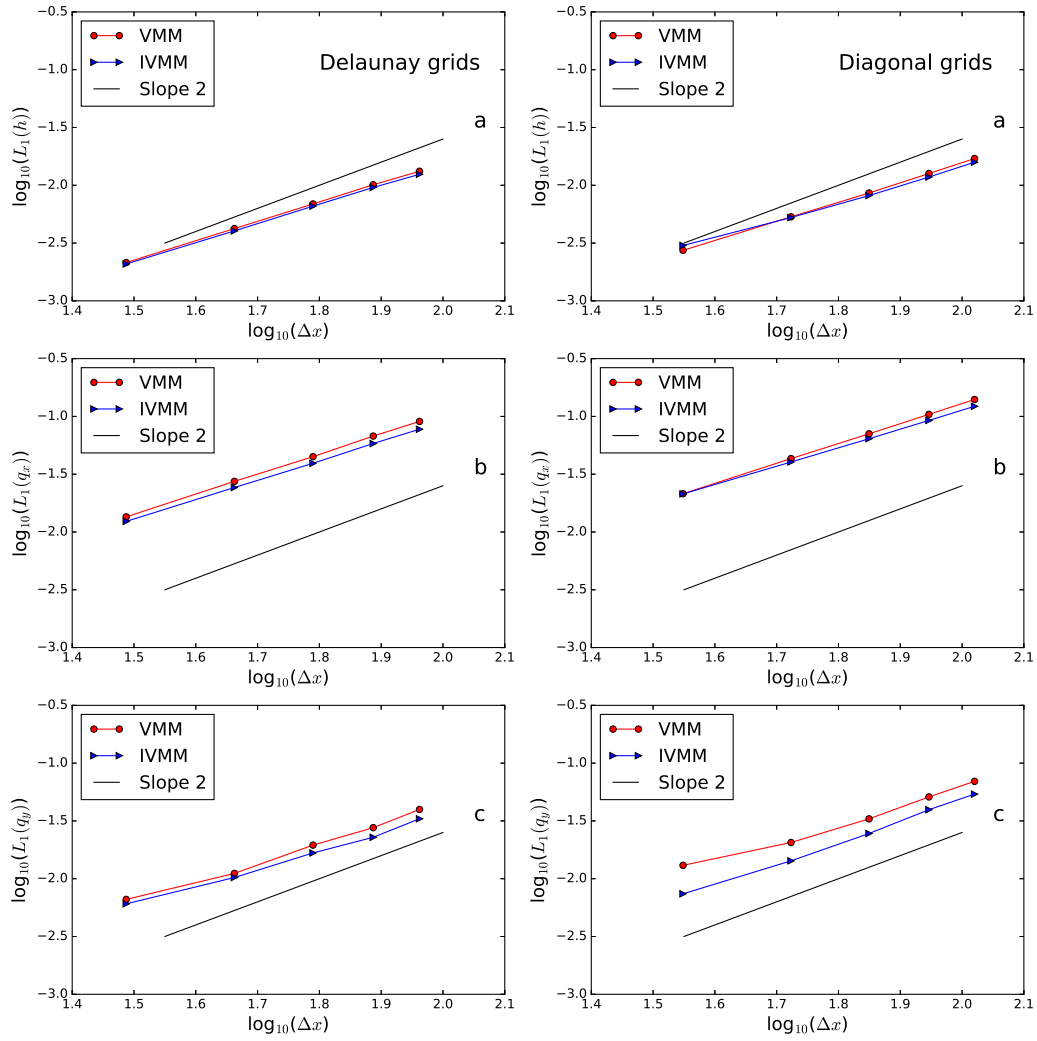


Figure 9: Moving shorelines in a two-dimensional frictional parabolic bowl: grid convergence study on Delaunay grids (left) and diagonal grids (right) for  $h$  (a),  $q_x$  (b) and  $q_y$  (c).



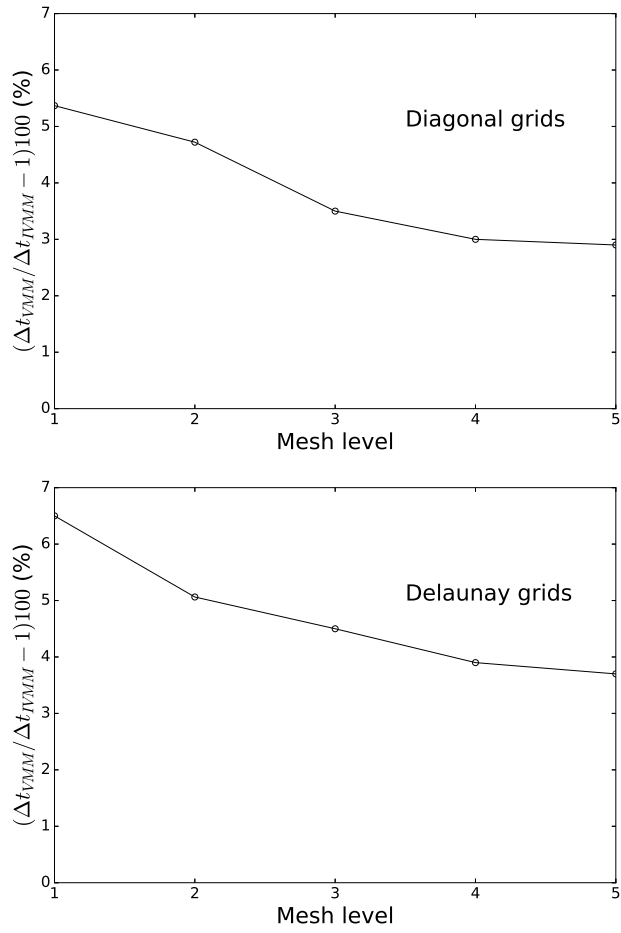


Figure 10: Moving shorelines in a two-dimensional frictional parabolic bowl: relative computational time for a single step for VMM scheme and IVMM scheme for the diagonal grids (upper) and Delaunay grids (lower).

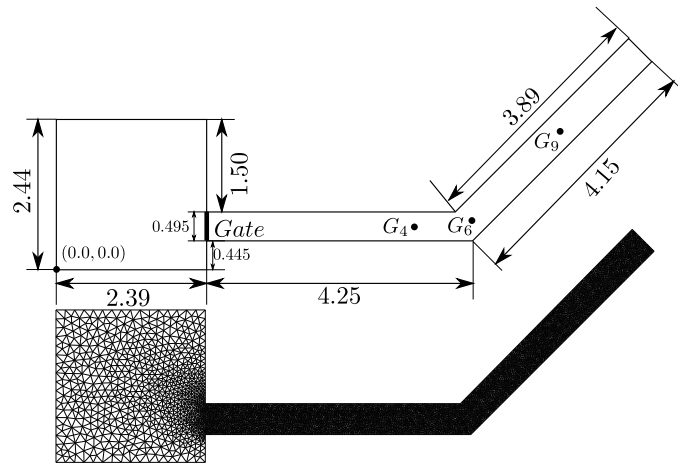


Figure 11: Dam-break in a channel with  $45^\circ$  bend: plan view of the experiment set up (upper) and the computational grid (lower), values in (m).

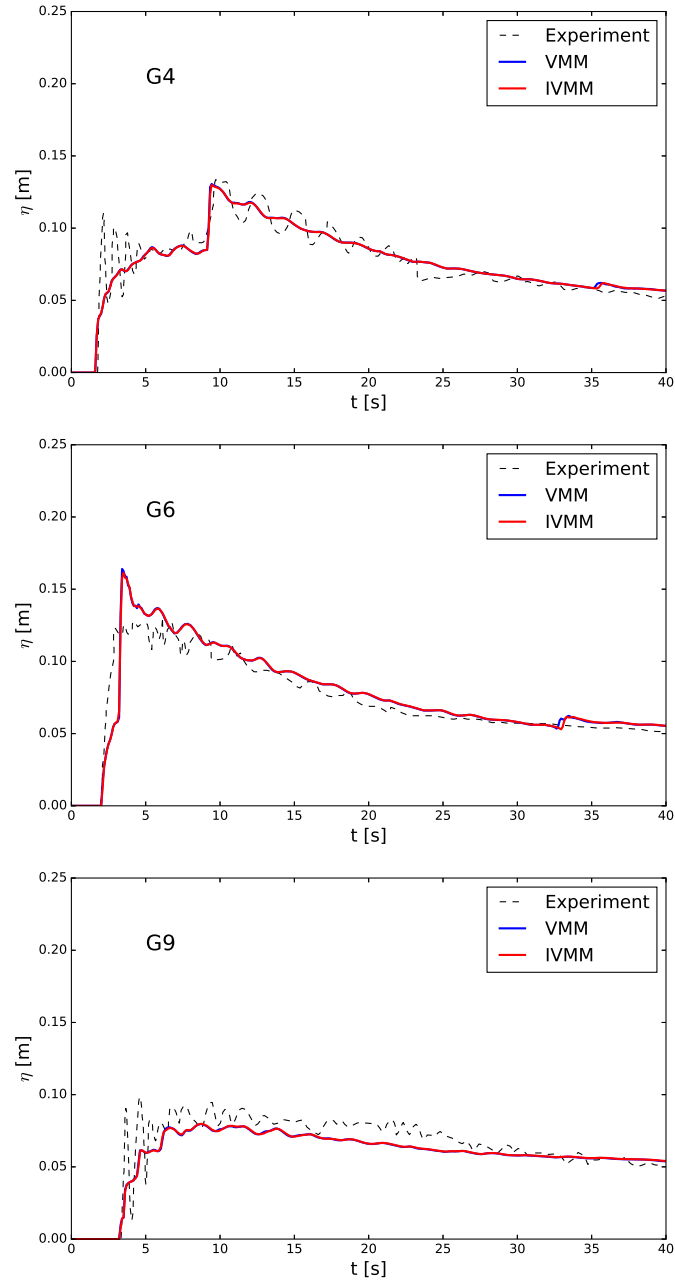


Figure 12: Dam-break in a channel with  $45^\circ$  bend: water level at G4 (upper), G6 (middle), G9 (lower) against measurements.

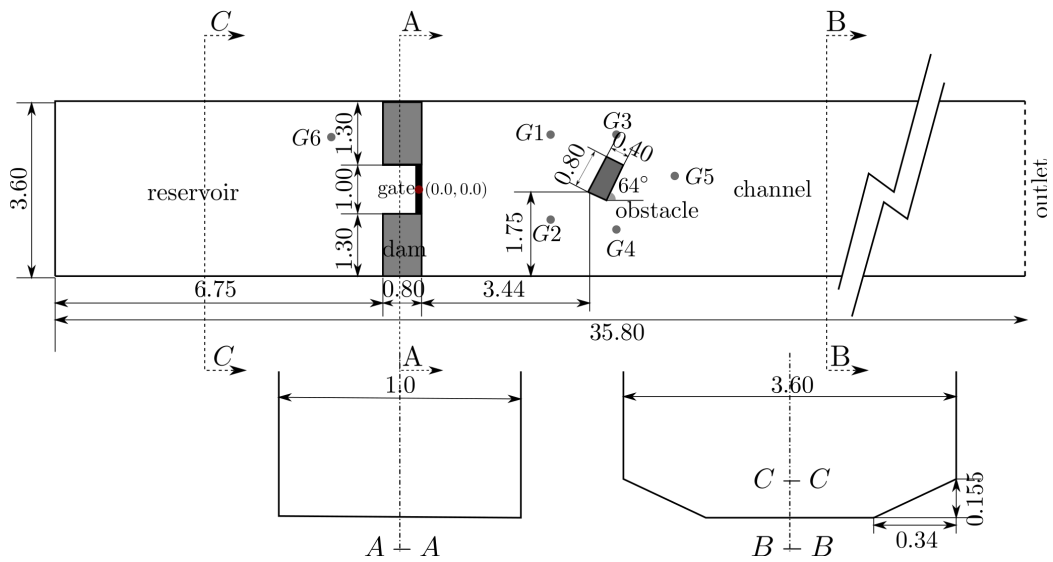


Figure 13: Two-dimensional dam-break flow against an isolated obstacle: sketch of the experiment set up (m) after [33].

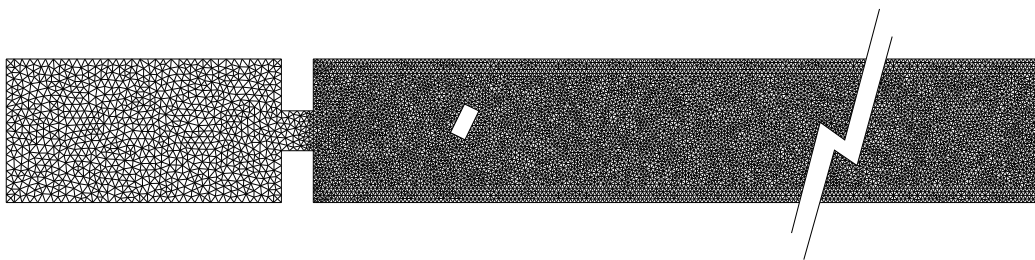


Figure 14: Two-dimensional dam-break flow against an isolated obstacle: computational grid used for simulation.

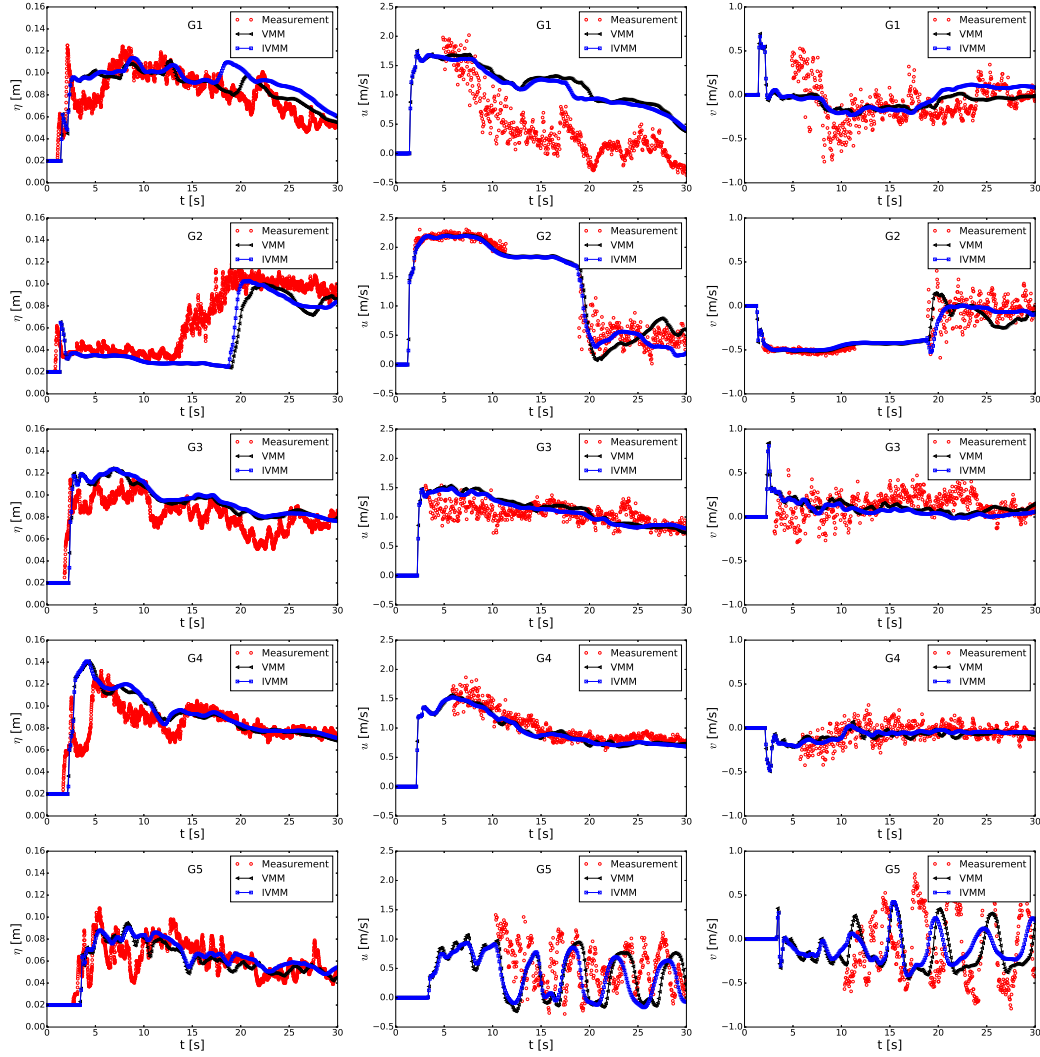


Figure 15: Two-dimensional dam-break flow against an isolated obstacle: the comparison of water elevation (left), the velocity along  $x$ - direction (middle) and  $y$ - direction (right) between measurement data ( $\circ$ ), and simulation results from VMM ( $\square - \square$ ) and IVMM ( $\triangleleft - \triangleleft$ ) at gauges G 1-5.

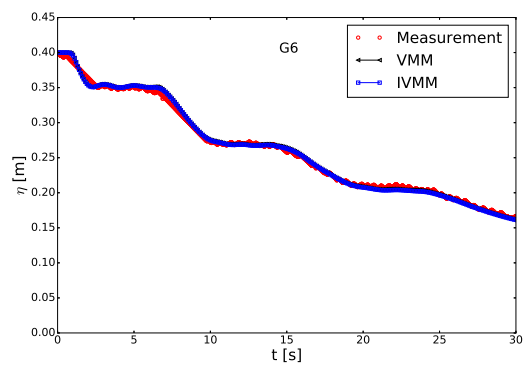


Figure 16: Two-dimensional dam-break flow against an isolated obstacle: the comparison of water elevation between measurement data ( $\circ$ ), and simulation results from VMM ( $\square$ ) and IVMM ( $\triangle$ ) at gauges G 6.

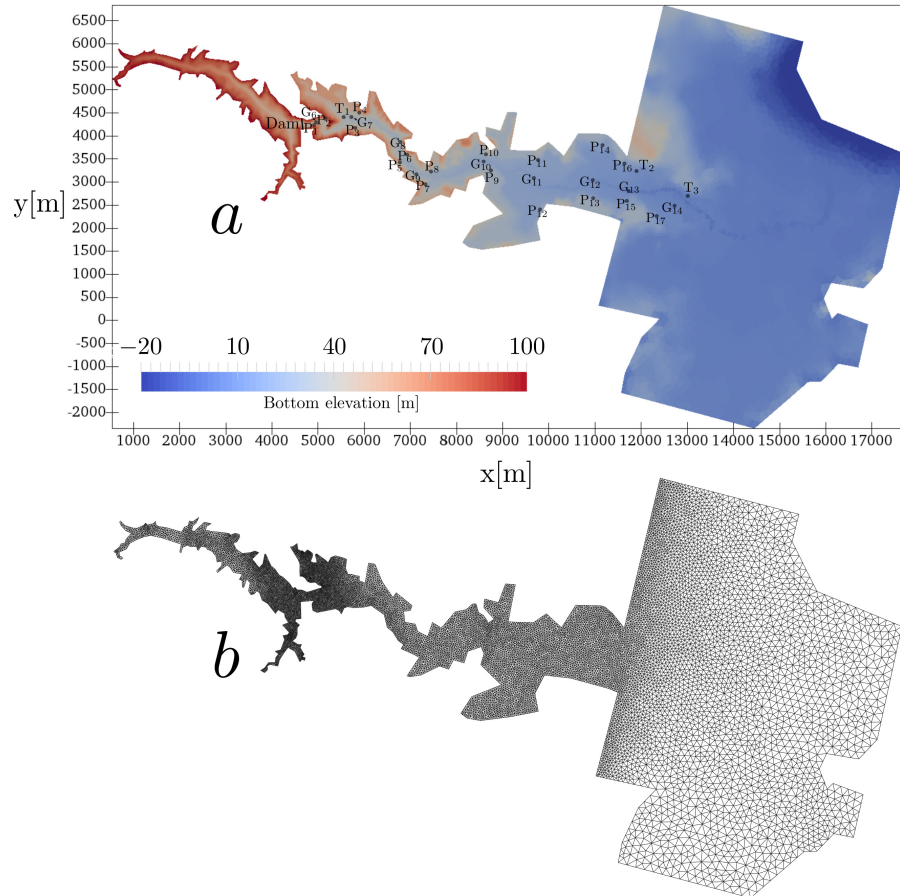


Figure 17: Malpasset dam-break: topography and locations of electrical transformers  $T$ , survey points  $P$  and experimental gauges  $G$  (a); computational domain and simulation grid (b).

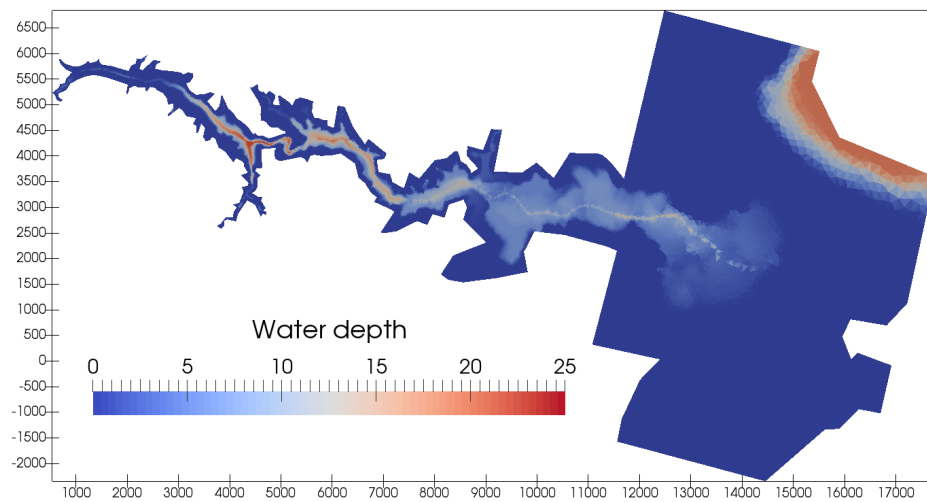


Figure 18: Malpasset dam-break: predicted water depth (m) by IVMM scheme at  $t = 2000$  s.



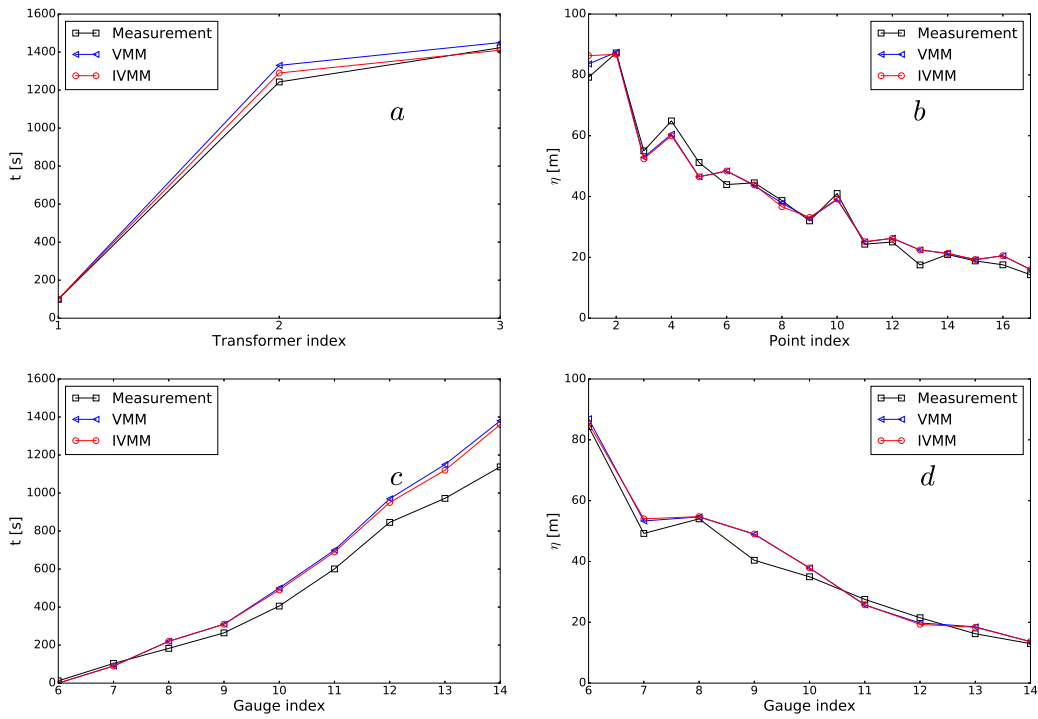


Figure 19: Malpasset dam-break: (a) arrival times at three electrical transformers, (b) maximum water levels at survey points, (c) arrival times at experiment gauges, (d) maximum water levels at experimental gauges.